

Physical and Dielectric Properties of Polycrystalline $\text{LaV}_{0.5}\text{Nb}_{0.5}\text{O}_4$

Ashok Kumar,^{1,2} Simranjot K. Sapra,³ Ramcharan Meena,⁴ Vinod Singh,¹ Anita Dhaka,⁵ and Rajendra S. Dhaka^{3,*}

¹Department of Applied Physics, Delhi Technological University, Delhi-110042, India

²Department of Physics, Atma Ram Sanatan Dharma College, University of Delhi, New Delhi-110021, India

³Department of Physics, Indian Institute of Technology Delhi, Hauz Khas, New Delhi-110016, India

⁴Material Science Division, Inter-University Accelerator Center, Aruna Asaf Ali Road, New Delhi-110067, India

⁵Department of Physics, Hindu College, University of Delhi, New Delhi-110007, India

(Dated: January 23, 2026)

We report a detailed investigation of the structural, electronic, vibrational, and dielectric properties of polycrystalline $\text{LaV}_{0.5}\text{Nb}_{0.5}\text{O}_4$ samples, prepared at two sintering temperatures (1000°C and 1250°C). The introduction of Nb^{5+} at the V^{5+} site leads to notable structural and vibrational changes, which can be attributed to their isoelectronic nature and the comparatively larger ionic radius of Nb^{5+} . The Rietveld refinement of the X-ray diffraction patterns confirms a coexistence of monoclinic ($P2_1/n$) and scheelite-type tetragonal ($I4_1/a$) phases; for example, with a fraction of 4% and 96% for the sample annealed at 1250°C . The particle morphology has altered from spherical (1000°C) to irregular-shaped (1250°C) as a result of increase in annealing temperature. The Raman spectroscopy, Fourier Transform Infrared spectroscopy and X-ray Photoemission Spectroscopy have been used to understand the vibrational and electronic properties. An optical band gap of 2.7 eV for the sample sintered at 1250°C is calculated using Ultraviolet-vis diffuse reflectance spectroscopy measurements. The dielectric studies shows the higher dielectric permittivity (ϵ_r) and lower dielectric loss for the sample annealed at 1250°C .

I. INTRODUCTION

In last few decades, rare-earth orthovanadates have emerged as a significant class of functional materials with broad environmental and industry applications spanning as luminescent materials, catalysis, solid oxide fuel cells, battery electrodes, thermometers and photocatalysts [1–5]. The orthovanadates with general formula RVO_4 , where R is a rare-earth ion, such as La^{3+} , Gd^{3+} , Y^{3+} etc., represent a versatile family of materials having the VO_4^{3-} tetrahedral units, which serve as the fundamental building blocks [6–9]. It allows the rare earth cations to form a crystal field, which upon perturbation, results in energy transition and phenomena of photoluminescence [10]. In the family, the lanthanum based orthovanadates, i.e., LaVO_4 has been considered most interesting due to its exceptional optical, electronic and structural properties [3] as well as used for targeted alpha therapy in cancer treatment through radionuclide encapsulation using ^{223}Ra to form $\text{La}(\text{Ra})\text{VO}_4$ [11]. Interestingly, the LaVO_4 exhibits peculiar structural polymorphism, crystallizing primarily in two structure types: the tetragonal (t-) zircon-type (space group $I4_1/\text{amd}$ [141]) and the monoclinic (m-) monazite-type (space group $P2_1/n$ [14]) [12, 13]. In the monoclinic monazite structure, La^{3+} ions are coordinated by nine oxygen atoms forming edge sharing LaO_9 polyhedra and connected with distorted VO_4 tetrahedra with four different V–O bond lengths. However, in the tetragonal zircon structure, La^{3+} ions are eight-fold coordinated with the equal V–O bond lengths and linked together through chains along the c -axis. Importantly, the LaVO_4 shows stability in monoclinic mon-

azite structure at room temperature with La^{3+} ion's high tendency to crystallize in nine-coordination as compared to the eight coordination in tetragonal zircon structure [12]. This is mainly because the phase stability is dependent on the cation radius and La^{3+} has the largest ionic radius (1.16 Å) as compared to other rare earth cations. The tetragonal (zircon-type) phase of LaVO_4 is metastable at room temperature, but can be synthesized through solution-based methods such as hydrothermal [12, 14]. Interestingly, the tetragonal structure exhibits superior luminescence properties due to the presence of four identical V–O bonds (angle $\approx 153^\circ$), which facilitate more efficient energy transfer [15]. In contrast, the monoclinic monazite phase has smaller bond angles, resulting in less effective energy transfer [15]. The LaVO_4 is a self-activated ABO_4 type host compound, emitting broad blue emission from 380 nm to 450 nm region with maxima at 430 nm upon UV light excitation. This corresponds to a transition from two close lying $^1\text{A}_1(^1\text{E})$ and $^1\text{E}_1(^1\text{T}_2)$ excited states to $^1\text{A}_2(^1\text{T}_1)$, ground state of $(\text{VO}_4)^{3-}$ ion [16]. Here, the Lanthanum is significantly more abundant and less expensive than Yttrium, making LaVO_4 -based materials economically attractive alternatives to the widely used YVO_4 phosphors [17]. This cost advantage is particularly important for large-scale applications in lighting and display technologies.

Notably, the structural diversity enables tunable optical and electronic properties through composition and external conditions such as pH, temperature and pressure [11, 12, 18]. Therefore, substitution at V^{5+} site in LaVO_4 has been explored through various dopants, such as Mn^{4+} where $\text{LaV}_{1-x}\text{Mn}_x\text{O}_{4-\delta}$ ($0 \leq x \leq 1$) mixed oxides were synthesized in single-phase with reproducible redox behavior (LaVO_4 to LaVO_3), which indicate that the Mn doping lowered reduction/oxidation temperatures and

* Corresponding author: rsdhaka@physics.iitd.ac.in

enhanced oxygen vacancy formation and mobility for catalytic performance [19]. Interestingly, substituting low-cost Nb^{5+} at the V^{5+} site in LaVO_4 motivated by the intriguing structural and optical behavior arising from the isoelectronic character (d^0 electronic configuration) and larger ionic radii of Nb^{5+} as compared to V^{5+} [5–7]. It has also been well-demonstrated that even small amounts of Nb^{5+} substitution ($x \geq 0.05$) can induce the formation of the scheelite-tetragonal phase ($I4_1/a$) alongside the monoclinic phase at room temperature [5]. The presence of the tetragonal phase significantly enhances photoluminescence properties and the structural transformation can be controlled by varying the Nb concentration [5–7]. Meanwhile, the end composition in the series, i.e., the LaNbO_4 is a rare-earth niobate and structurally transforms from monoclinic fergusonite ($I2/a$) to tetragonal scheelite ($I4_1/a$) at 495°C [20]. On the other hand, Ding *et al.* reported the LaNbO_4 in monoclinic phase, which exhibits interesting luminescent features with fluorescence lifetime of $5.51\ \mu\text{s}$ [21]. In a similar fashion, when V^{5+} ion is substituted at the Nb^{5+} , the composition induced structural transition is observed [22]. Upon excitation with a UV or X-ray source, charge transfer from $\text{O}\ 2p$ to $\text{Nb}\ 4d$ band in LaNbO_4 yielded a blue luminescent material, as demonstrated by Blasse *et al.* in ref. [23]. However, the composition $\text{LaV}_{0.5}\text{Nb}_{0.5}\text{O}_4$ remains largely unexplored and presents significant scope for detailed investigation particularly to see the effect of sintering temperature during the synthesis process as well as temperature dependent dielectric properties [5–7].

Therefore, the primary aim of this work is to study polycrystalline lanthanum orthovanadate with niobium substitution, specifically targeting the composition $\text{LaV}_{1-x}\text{Nb}_x\text{O}_4$ where x equals 0.5, utilizing the solid-state method and investigate sintering temperature induced phase transformation and understand the dielectric properties. Interestingly, the crystal structure and morphology of the orthovanadates is strongly dependent upon the synthesis approach, annealing temperature and concentration of active ions. Herein, the $\text{LaV}_{0.5}\text{Nb}_{0.5}\text{O}_4$ sample crystallize in two distinct, monoclinic monazite type and tetragonal zirconite type phases in different fractions, as confirmed by the Rietveld refinement of X-ray diffraction (XRD) patterns. The scanning electron microscopy (SEM) measurements unveil the morphological variations with the sintering temperature. The Raman spectroscopy and Fourier transform infrared spectroscopy (FTIR) measurements identify the presence of vibrational bonds in the prepared samples. The energy band gap values have been estimated through ultraviolet-visible diffuse reflectance spectroscopy measurements. The core-level X-ray photoemission spectroscopy studies depict the electronic structure and oxidation state of the constituent elements in both the samples. The microstructure has been successfully confirmed by the high-resolution transmission electron microscopy measurements. The dielectric measurements reveal the dielectric permittivity (ϵ_r) and dielectric loss in the temper-

ature range of 100 K to 400 K for the samples annealed at 1000°C and 1250°C . The *a.c.* conductivity studies are performed to understand the charge carrier dynamics with variable temperature and frequencies.

II. EXPERIMENTAL

Materials Preparation: The $\text{LaV}_{0.5}\text{Nb}_{0.5}\text{O}_4$ bulk sample was synthesized via a conventional solid-state reaction route. Prior to synthesis, La_2O_3 was pre-heated at 900°C for 6 h with a ramp rate of $4\ ^\circ\text{C}\ \text{min}^{-1}$ in order to remove the adsorbed moisture. The calcined La_2O_3 was quenched to room temperature and weighed immediately to prevent re-hydration. High-purity La_2O_3 , V_2O_5 , and Nb_2O_5 were mixed in the stoichiometric ratio to obtain a 2 g final yield of the powder. The precursors were thoroughly mixed and ground in an agate mortar and pestle for 6 hr to ensure homogeneous mixing. The resulting powder was pelletized under a uniaxial pressure of $1500\ \text{kg}\ \text{cm}^{-2}$, followed by calcination at 1000°C for 17 hr with a heating rate of $5^\circ\text{C}\ \text{min}^{-1}$. The calcined product was reground for approximately 5 hr to ensure homogeneity and subsequently re-pelletized under the same applied pressure ($1500\ \text{kg}\ \text{cm}^{-2}$). The final sintering was carried out at 1250°C for 13 hr with a ramp rate of $5^\circ\text{C}\ \text{min}^{-1}$. The $\text{LaV}_{0.5}\text{Nb}_{0.5}\text{O}_4$ samples annealed at 1000°C and 1250°C are abbreviated as LVNO-1000 and LVNO-1250, respectively.

Physical and Dielectric characterizations: The X-ray diffraction (XRD) measurements are carried out using a Panalytical X'Pert³ diffractometer equipped with $\text{Cu}\ K_\alpha$ radiation ($\lambda = 1.5406\ \text{\AA}$). The Rietveld refinement of the powder XRD patterns is performed using the FullProf software, with the background fitted using linear interpolation between the data points. The morphology of the bulk samples is examined using a field-emission scanning electron microscope (FE-SEM, Tech-nai Magna LMU). The elemental mappings are probed through the EDX detector system (EDAX AMETEK, Octane Elite Super EDS). The Fourier-transform infrared spectroscopy (FTIR, Thermo Nicolet IS-50) is performed in Attenuated Total Reflectance (ATR) mode over the spectral range of $400\text{--}4000\ \text{cm}^{-1}$ to analyse vibrational modes. The X-ray photoelectron spectroscopy (XPS, Kratos AXIS Supra) is employed to investigate the valence state using monochromatic $\text{Al}\ K_\alpha$ radiation (1486.6 eV) as the excitation source, with a pass energy of 20 eV and a step size of 0.1 eV. The spectral fitting is performed using FitYk software with Voigt function (Shape factor = 0.6), and the C 1s peak at 284.6 eV was used as the reference for calibration. The microstructure of the bulk samples is examined using transmission electron microscopy (TEM, JEM-ARM200F NEOARM). The Raman spectroscopy is performed using a Renishaw inVia confocal Raman microscope equipped with a 532 nm laser, a 2400 lines/mm grating, and a laser power of 10 mW to investigate the vibrational modes of the sam-

plexes. The UV-vis (Ultraviolet-visible) diffuse reflectance spectroscopy (DRS) measurements are conducted using a Perkin Elmer's Lambda 1050 model in the spectral range of 300–2500 nm to measure the absorption edge energy of the samples using the Barium Sulfate standard. The pellets were polished and painted with silver paste on both the sides for the dielectric measurements. The dielectric studies are done in the temperature range of 90–400 K by varying the frequency from 100 Hz–2 MHz using the Agilent LCR meter (model E4980A). The temperature is varied using the Lakeshore temperature controller (model-340) and temperature was measured using the Pt-100 sensor. The measurements are performed in the vacuum of the order 10^{-2} mbar by placing the sample holder in liquid nitrogen Dewar.

III. RESULTS AND DISCUSSION

The room temperature Rietveld refined XRD patterns of as-prepared polycrystalline $\text{LaV}_{0.5}\text{Nb}_{0.5}\text{O}_4$ samples, annealed at 1000°C and 1250°C are depicted in Figs. 1(a, b), respectively. It is observed that the measured XRD pattern consists of a mixture of monoclinic ($P2_1/n$) and scheelite-tetragonal ($I4_1/a$) phases in varying proportions, rather than a single $P2_1/n$ phase [22]. The structural phase transformation in the LVNO sample is caused by the Nb^{5+} substitution at the V^{5+} site in a tetrahedral coordination, because the ionic radius of Nb^{5+} (0.48 Å) is larger than that of V^{5+} (0.355 Å) [24]. It is also reported in the literature that end members, the LaVO_4 and LaNbO_4 co-exist in the monoclinic monazite ($P2_1/n$) and fergusonite monoclinic ($I2/a$) phases, respectively, at room temperature [25, 26]. Consequently, it is anticipated that Nb^{5+} substitution in LaVO_4 will induce a phase transformation from $P2_1/n$ to $I2/a$. In the LaVO_4 sample, synthesized at 1000°C, the XRD pattern is well fitted using monoclinic ($P2_1/n$) and scheelite-tetragonal ($I4_1/a$). The phase exhibits diffraction peaks characteristic of a crystalline solid; however, the peaks appear relatively broad and of lower intensity compared to those of the sample sintered at 1250°C. This broadening indicates a reduced degree of crystallinity and/or smaller crystallite size in the LVNO-1000 sample. In contrast, the LVNO-1250 sample displays sharp and intense diffraction peaks, signifying enhanced crystallinity and larger crystallite dimensions, as shown in Fig. 1(b). The higher synthesis temperature likely promotes more complete crystallization and grain growth. The diffraction peaks for both the samples sintered at 1000°C and 1250°C correspond to two structural phases: the scheelite-type tetragonal phase ($I4_1/a$) and the monoclinic phase ($P2_1/n$).

The lattice parameters and wyckoff positions of LVNO-1000 and LVNO-1250 samples are summarized in Table I and Table II, respectively. It is observed that angle β has slightly increased with increase in sintering temperature, as a result of increase in tetragonal phase fraction. The quantification of the relative phase fractions for

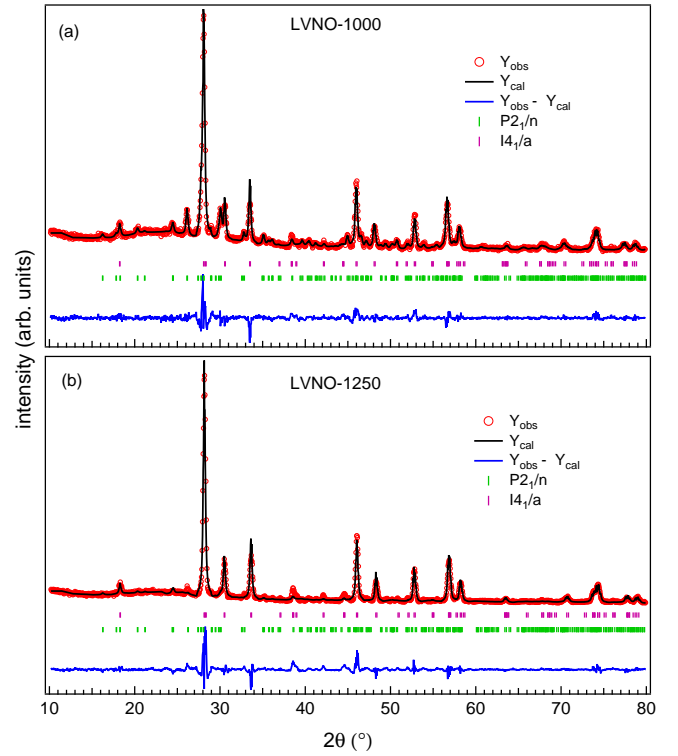


FIG. 1. The room temperature XRD patterns with Rietveld refinement of (a) LVNO-1000 and (b) LVNO-1250 samples. The open red circles, black solid line, and blue solid line exhibits the experimental, calculated, and the difference between experimental and calculated pattern, respectively. The vertical green and purple markers show the Bragg positions corresponding to the $P2_1/n$ and $I4_1/a$ space groups.

TABLE I. The structural and atomic parameters obtained from Rietveld refinement of the sample sintered at 1000°C.

Tetragonal Phase: $a = b = 5.348$ Å, $c = 11.694$ Å					
Atom	x	y	z	Occ.	Site
Nb	0.0000	0.0000	0.0000	1.00	36f
O	0.2635	0.8049	0.1435	1.00	36f
La	0.0000	0.0000	0.5000	1.00	6b
Monoclinic Phase: $a = 7.054$ Å, $b = 7.278$ Å, $c = 6.731$ Å $\beta = 104.909^\circ$					
Atom	x	y	z	Occ.	Site
V	0.3071	0.1657	0.6066	1.00	36f
O1	0.2438	0.0155	0.4594	1.00	36f
O2	0.3676	0.3134	0.5676	1.00	36f
O3	0.4553	0.0593	0.8394	1.00	6b
O4	0.1324	0.2049	0.7648	1.00	18e
La	0.2723	0.1613	0.1128	1.00	18e

both the samples has also been investigated through Rietveld refinement. The phase fractions of 51% tetragonal ($I4_1/a$) and 49% monoclinic ($P2_1/n$) are calculated for the LVNO-1000 sample. On the other hand, the LVNO-1250 sample exhibits a dominant tetragonal fraction of

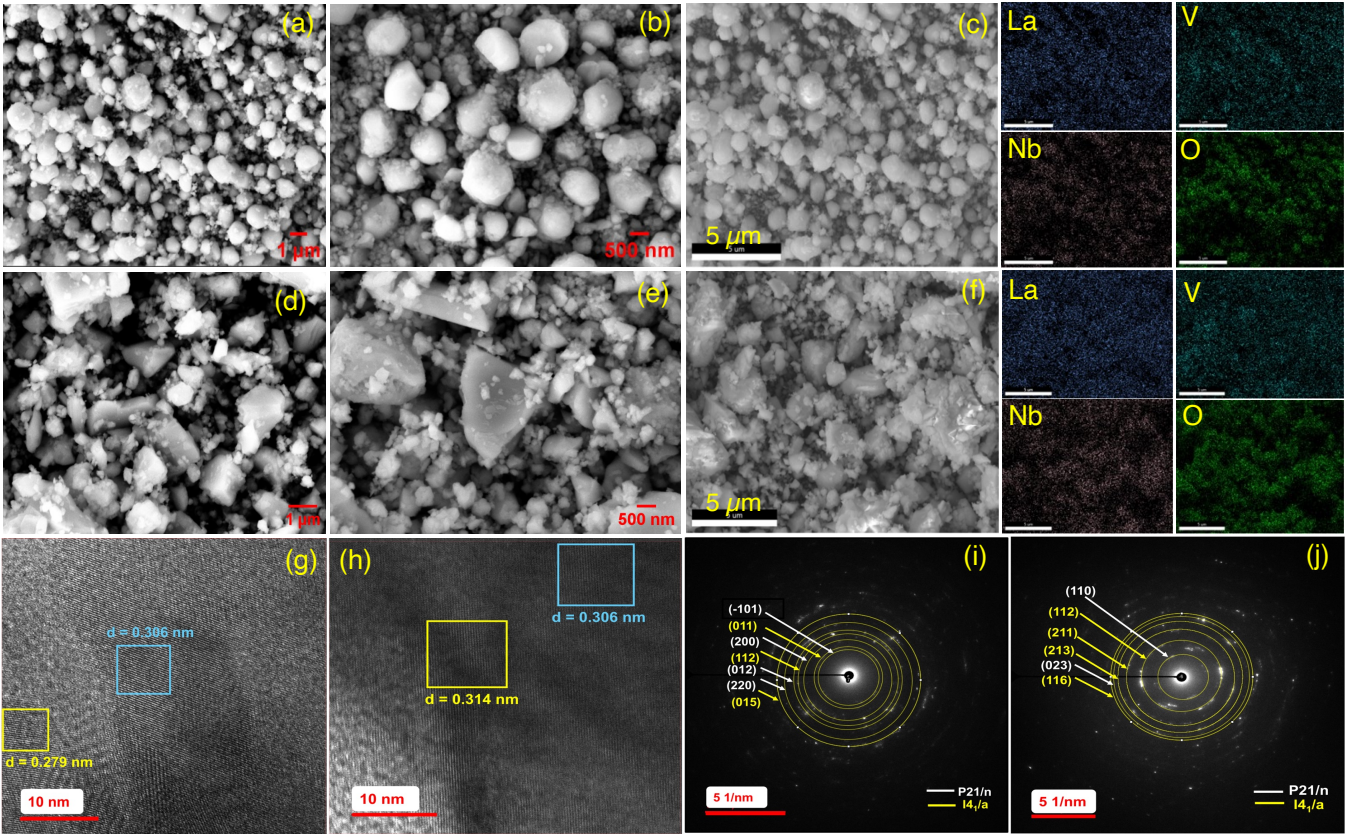


FIG. 2. The FE-SEM images of the LVNO-1000 sample at (a) $1\mu\text{m}$, (b) 500 nm and (c) probed region of scan (at $5\mu\text{m}$) with the corresponding elemental mappings of all elements; the FE-SEM images of the LVNO-1250 sample at (d) $1\mu\text{m}$, (e) 500 nm and (f) probed region of scan (at $5\mu\text{m}$) with the corresponding elemental mappings of all elements; the HR-TEM images of (g) sintered at 1000°C and (h) sintered at 1250°C with the marked d -spacings across the selected region; the SAED patterns for the LVNO-1000 (i) and LVNO-1250 (j), respectively.

TABLE II. The Structural and atomic parameters obtained from Rietveld refinement of LVNO sintered at 1250°C .

Tetragonal Phase: $a = b = 5.327\text{ \AA}$, $c = 11.716\text{ \AA}$					
Atom	x	y	z	Occ.	Site
Nb	0.0000	0.0000	0.0000	1.00	36f
O	0.2500	0.7682	0.1576	1.00	36f
La	0.0000	0.0000	0.5000	1.00	6b
Monoclinic Phase: $a = 7.027\text{ \AA}$, $b = 7.293\text{ \AA}$, $c = 6.732\text{ \AA}$ $\beta = 104.947^\circ$					
Atom	x	y	z	Occ.	Site
V	0.3024	0.1699	0.5733	1.00	36f
O1	0.1951	0.0846	0.4725	1.00	36f
O2	0.5818	0.3642	0.5407	1.04	36f
O3	0.8340	0.1151	0.7265	0.95	6b
O4	0.0960	0.6676	0.2146	0.76	18e
La	1.6958	0.2865	0.1337	1.00	18e

96% and a monoclinic fraction of 4%. The predominance of the tetragonal phase at the higher temperature

is consistent with its thermodynamic stability and structure becomes more homogeneous through completion of solid-state reaction. This is consistent with the previous work, where sintering of $\text{LaV}_{1-x}\text{Nb}_x\text{O}_4$ ($x = 0.1, 0.2$) at 1450°C promoted the stabilization of scheelite-tetragonal phase [5]. In addition, Xie *et al.* reported the mechanism of formation of tetragonal phase as a result of intermediate complex $\text{V}_x\text{O}_y^{(2y-5x)-}$, which forces La^{3+} to coordinate in fewer coordination value (here, 8) due to strong stearic hindrance [27]. This increment in tetragonal phase fraction is better for superior luminescent characteristics [28].

The FE-SEM images of the LVNO samples, sintered at 1000°C and 1250°C are presented in Figs. 2(a-f). The LVNO-1000 sample shows an average particle size of approximately $0.8\text{ }\mu\text{m}$. In contrast, the LVNO-1250 sample exhibits a non-uniform particle size distribution ranging from $0.2\text{ }\mu\text{m}$ to several micrometers, as depicted in Fig. 2(b). The grain size has increased with the increase in sintering temperature, as the shape changing from spherical (at 1000°C) to irregular-shaped (at 1250°C) particles. The morphological difference along with the visible textural changes, such as inevitable agglomera-

tion in the LVNO-1250 sample, provide additional evidence of the temperature-induced phase transformation. The grain boundaries diffuse, smaller particles rearrange to large sized particles and coalescence occurs as a result of high temperature annealing [29]. Furthermore, the uniform distribution of elements in LVNO-1000 and LVNO-1250 samples can be clearly observed in Figs. 2(c, f). The HR-TEM analysis of the LVNO-1000 sample clearly reveals its biphasic nature, with distinct coexisting lattice fringes exhibiting *d*-spacings of approximately 0.28 nm and 0.3 nm, depicted in Fig. 2(g). The indexed (h, k, l) planes that relate to $P2_1/n$ and $I4_1/a$ are colored in white and yellow, respectively, see Figs. 2(g, h). The corresponding SAED pattern further confirms the mixed phase structural arrangement, where the reflections (-101), (200), (012) and (220) belong to the monoclinic phase and (011), (112) and (015) belong to the tetragonal phase, see Figs. 2(i, j). For the LVNO-1250 sample, the HR-TEM images indicate a dominant tetragonal phase [see Fig. 2(h)], with measured *d*-spacings shifting to around 0.31 nm, which are characteristic of the major tetragonal reflections. The SAED pattern for this sample is overwhelmingly dominated by diffraction spots consistent with the $I4_1/a$ phase, including the (112), (211), and (213) reflections [see Fig. 2(j)], providing strong evidence that higher sintering temperature promotes the stabilization and predominance of the tetragonal phase. This is in agreement with the refined X-ray diffraction analysis, presented in Figs. 2(a, b).

In order to confirm the structure and possibility of infrared active modes of the $\text{LaV}_{0.5}\text{Nb}_{0.5}\text{O}_4$ sample, the ATR-FTIR measurements have been performed, as depicted in Fig. 3(a), with the closer view shown in the inset. The observed well-resolved bands are marked with the black vertical arrows [inset of Fig. 3(a)] and are in close agreement with ref. [5]. Herein, a strong and distinct band is observed at 432 cm^{-1} , with a weak band at 478 cm^{-1} , which are linked to the ν_4 bending vibrations of the $(\text{V}/\text{Nb})\text{O}_4^{3-}$ tetrahedra [3]. Similarly, wide bands are observed between $600\text{--}900\text{ cm}^{-1}$, where a peak at 804 cm^{-1} corresponds to the antisymmetric stretching vibrations of VO_4^{3-} tetrahedra. Meanwhile, the peaks at 820 , 835 and 848 correspond to the ν_3 stretching vibrations of VO_4^{3-} tetrahedra [30] and show a small shift in the peaks in comparison to pristine LaVO_4 sample [5]. In addition, the peaks at 679 , 729 and 761 cm^{-1} have been originated with the incorporation of Nb at V site and are absent in the LaVO_4 sample. These features can be correlated with the additional symmetry modes, arising from the mixed scheelite-tetragonal phase, as proven in X-ray diffraction measurements. However, the ATR-FTIR spectra for LVNO-1250 sample shows less intense band around 417 cm^{-1} , while the peaks in the range of $600\text{--}900\text{ cm}^{-1}$ appear as a single broad band, depicted in Fig. 3(a). It can be inferred that IR activity gets reduced with increasing temperatures due to increase in thermal energy and as a result, intensity of specific vibrational bands are reduced.

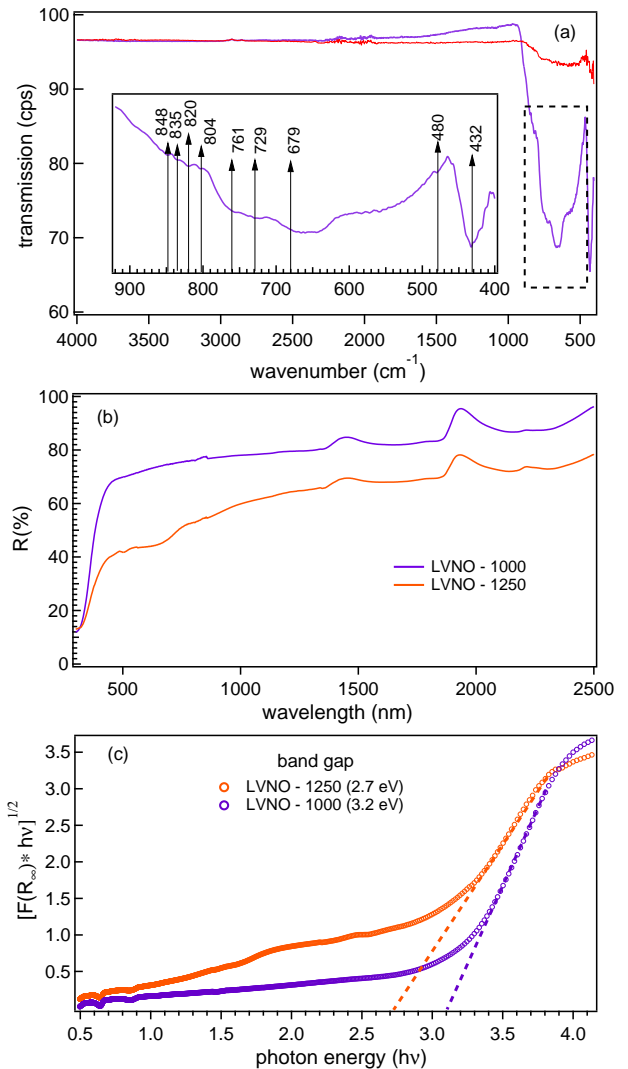


FIG. 3. (a) The FTIR spectra, (b) the UV-vis DRS plots and (c) the Kubelka-Munk plots obtained from the DRS data for the LVNO-1000 and LVNO-1250 samples, respectively.

The UV-vis DRS measurements are conducted to understand the absorption edge energy of the synthesised LVNO samples, sintered at 1000°C and 1250°C . The reflectance spectra [see Fig. 3(b)] observed for both the samples is converted to Tauc plot using the Tauc method [31]. The diffuse reflectance spectra (DRS) are employed to calculate the Kubelka-Munk (K-M) function $[F(R_\infty)]$, shown in Fig. 3(c), which can be treated in terms of diffuse semi-infinite reflectance ($R_\infty = R_{\text{sample}}/R_{\text{standard}}$) as written below [32]:

$$F(R_\infty) = \frac{(1 - R_\infty)^2}{2R_\infty} \quad (1)$$

The band gap of the LVNO samples can be obtained from the absorption threshold energy, which is the *x*-axis intercept of the Tauc plot [see Fig. 3(c)] and related as [33]:

$$(ah\nu) = k(h\nu - E_g)^\eta \quad (2)$$

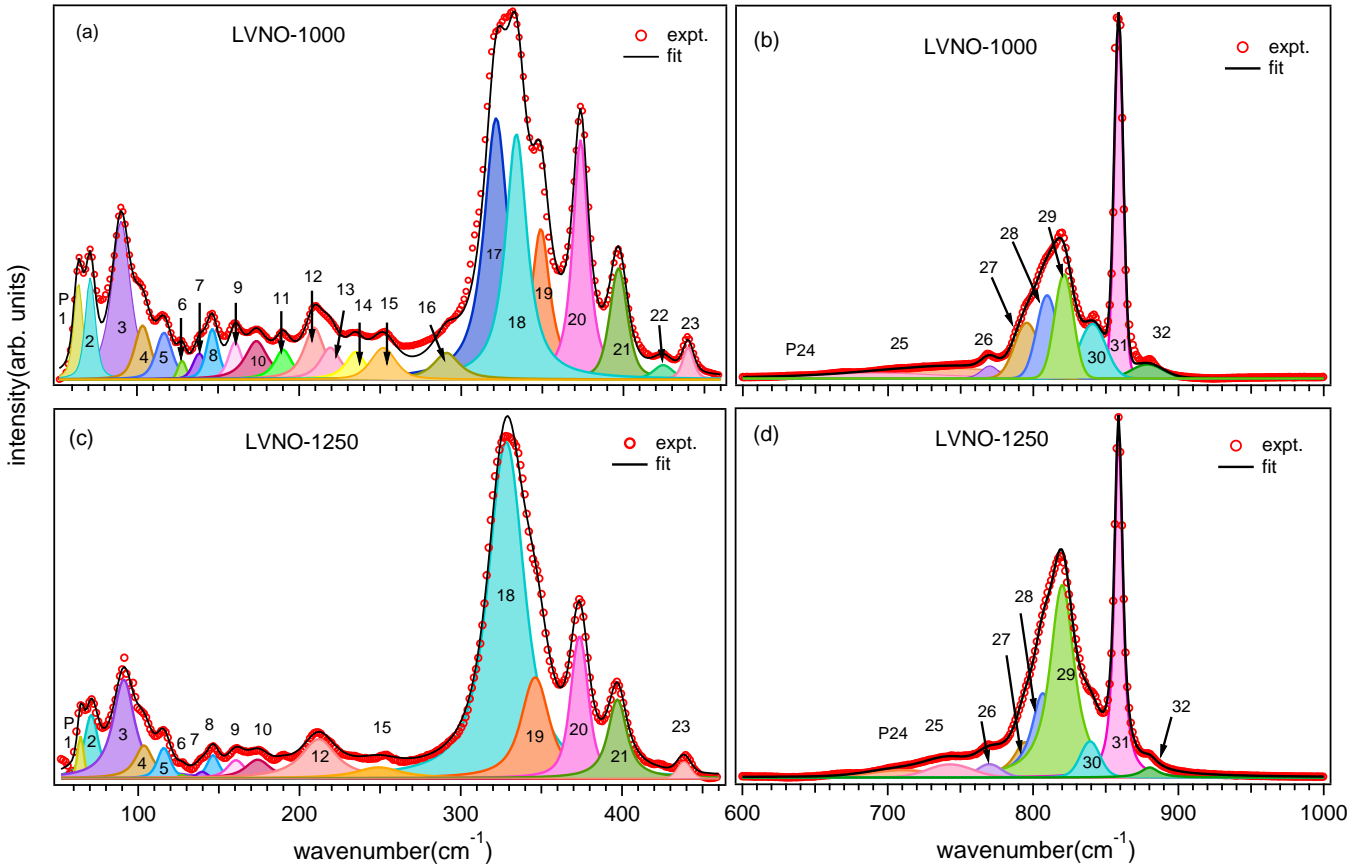


FIG. 4. The room temperature Raman spectra of LVNO sample, (a, b) sintered at 1000°C and (c, d) for sample sintered at 1250°C in the low and middle wavenumber regions, respectively; fitted using the Voigt peak function and solid thick black line presents the total fit of the measured spectra.

where α , ν , k , E_g and η are the absorption coefficient, frequency, absorption constant, band gap energy and exponent of the equation, respectively [34]. The value of the exponent η depends on the type of the transition/band gap in the material and can have values of 1/2, 2, 3/2 and 3 for the direct allowed, indirect allowed, direct forbidden and indirect forbidden transitions, respectively [31, 34]. However, in the case of diffuse reflectance spectra, the α in Tauc plot can be replaced by the K-M function to estimate the band gap of the material [3]. As reported in [5], the LVNO samples has indirect band gap, therefore, the value of exponent, η is 2, therefore, $[F(R_\infty) \times h\nu]^{1/2}$ versus $h\nu$ is plotted for both the samples, shown in Fig. 3(c). This curve shows the linear and non-linear portions which are the characteristics for allowed transitions. The linear portion of the curve which lies in the range approximately 3 eV to 4.5 eV characterizes the fundamental absorption of the materials and the non-linear portion of the curve correspond to a residual absorption, which involves defect states. The x -axis intercept along the optical absorption edge of the samples estimates the optical band gap, which is calculated as 3.2 and 2.7 eV for the 1000°C and 1250°C, respectively. Also, Sun *et al.* reported that monoclinic LaVO₄ phase possess indi-

rect band gap of 3.5 eV, while tetragonal phase has direct band gap of 3 eV through the first-principle calculations [35]. Therefore, it can be clearly inferred that band gap decreases upon increasing the sintering temperature, as a result of increase in tetragonal phase in LVNO-1250 sample and further enhances the photoluminescence. This is also in agreement with the previously reported literature [3, 5, 33].

Moreover, the Raman spectra recorded at a room temperature using a 532 nm excitation laser line for both the samples are presented in the Fig. 4(a-d). A Voigt profile function is employed to deconvolute and fit the observed Raman modes, as mentioned in the Table III. The intensity of observed Raman modes may fluctuate due to various factors, including the molecule's polarizability, the excitation wavelength of the laser source, and the concentration of the active groups [6]. The detailed description of the various types of Raman modes has been discussed in our previous works [5, 6]. As per the group theory calculations reported, m-LaVO₄ consists of 72 vibrational modes ($18B_u + 18A_u + 18A_g + 18B_g$), which includes 3 acoustic modes ($A_u + 2B_u$), 33 infrared-active modes ($16B_u + 17A_u$), and 36 Raman active modes ($18A_g + 18B_g$) [35]. In this context, we employ Mulliken sym-

TABLE III. The peak fitting parameters for the observed vibrational frequencies (ω_{obs}) of the LVNO-1000 and LVNO-1250 samples at room temperature in the wavenumber regions (50–1000 cm⁻¹).

Sample	LVNO-1000	LVNO-1250
Peak	ω_{obs}	ω_{obs}
P1	$A_g(63.8)$	$A_g(64.2)$
P2	$A_g(71.2)$	$A_g(70.9)$
P3	$B_{1u}(90.2)$	$B_{1u}(91.0)$
P4	$B_g(103.5)$	$B_g(103.)$
P5	$B_{1g}(116.7)$	$B_{1g}(115.9)$
P6	$B_g(127.8)$	$B_g(127.0)$
P7	$E_g(138.4)$	$E_g(139.6)$
P8	$A_{2g}(146.8)$	$A_{2g}(146.4)$
P9	$B_g(159.8)$	$B_g(160.6)$
P10	$A_g(173.4)$	$A_g(174.1)$
P11	$A_g(189.8)$	$A_g(189.7)$
P12	$B_g(209.8)$	$B_{1g}(211.9)$
P13	$B_g(219.9)$	
P14	$A_g(232.8)$	
P15	$B_{2g}(251.6)$	$B_{2g}(249.1)$
P16	$B_g(285.6)$	
P17	$A_{1u}(320.0)$	
P18	$A_g(332.0)$	$A_{1g}(328.2)$
P19	$E_g(347.7)$	$E_g(346.2)$
P20	$A_g(373.6)$	$A_g(373.6)$
P21	$B_g(396.9)$	$B_g(397.2)$
P22	$A_g(423.4)$	
P23	$B_g(439.9)$	$B_g(438.5)$
P24	693.3	$A_g(710.3)$
P25	$B_g(747.7)$	$B_g(742.9)$
P26	$A_g(770.0)$	$A_g(769.9)$
P27	$B_g(795.5)$	$B_g(794.4)$
P28	$A_g(809.5)$	$A_g(806.7)$
P29	$A_g(821.1)$	$A_g(820.0)$
P30	$A_g(840.8)$	$A_g(839.3)$
P31	$B_g(858.8)$	$B_g(858.8)$
P32	$B_g(878.5)$	$B_g(880.2)$

bols, with notations A and B indicating that the vibrations are symmetric and anti-symmetric relative to the major axis of symmetry, respectively. The subscripts *g* and *u* denote that the vibrations are symmetric and anti-symmetric, respectively, concerning a center of symmetry. Meanwhile, the vibrational frequencies of tetragonal LaVO₄ (t-LaVO₄) consists of 36 vibrational modes and 33 zone-center optical phonon modes, with five E_g , four E_u , four B_{1g} , three A_{2u} , two A_{1g} , two B_{2u} , and one each of the A_{1u} , A_{2g} , B_{1u} , and B_{2g} symmetry representations. Among these, the A_{2u} and E_u modes are infrared active, whereas the A_{1g} , B_{1g} , B_{2g} , and E_g modes are Raman active. However, the remaining A_{1u} , A_{2g} , B_{1u} , and B_{2u}

modes are silent. The Raman, A_g , and B_g modes can be experimentally identified by polarized Raman measurements. The detailed description of the modes can be referred to references in [6, 35, 36].

The Raman modes in the lower wavenumber region for the LVNO-1000 and LVNO-1250 samples are presented as P0 to P23 and P24 to P32, respectively, in Fig. 4. Meanwhile, the corresponding details of Raman modes are described in Table III. In the LaV_{0.5}Nb_{0.5}O₄, the Raman peaks appear as a result of various vibrational bonds among La³⁺, V⁵⁺, Nb⁵⁺ and O²⁻. The Raman modes in the wavenumber region (600–800 cm⁻¹) are related to the stretching vibrations of O–(V/Nb)–O bonds and modes (300–450 cm⁻¹) correspond to the bending vibrations of O–V–O bonds and deformation/scissior modes of NbO₄³⁻ [6]. The Raman modes in the low wavenumber region are associated with the translational lattice modes of La (due to its lower mass) and rotational modes of NbO₄³⁻ [35]. Here, the P6 mode at 127.8 and 127.0 cm⁻¹ in LVNO-1000 and LVNO-1250 is linked with the translational motion of La atoms in the monoclinic phase. The P8 mode in the higher wavenumber region, located at 858.8 cm⁻¹ is the most intense mode, while the intensity of P6 mode enhanced with increase in temperature.

Herein, the peak (P12) at 209.8 cm⁻¹ assigned to the A_g mode corresponds to the torsional vibration of the VO₄ units, with the La atoms remaining nearly stationary. The peaks at 334 cm⁻¹ (P17) and 400 cm⁻¹ (P20) are attributed to A_g modes associated with the bending vibrations of the O–V–O bonds. Furthermore, the peak observed at 839 cm⁻¹ (P30) corresponds to the A_g mode, from the stretching vibrations of the O–V–O bonds. Furthermore, the presence of P8, P9, P10, P13, P14, P15, P17 and P18 modes confirms the existence of VO₄³⁻ ion because none of these modes are visible in LaNbO₄ [36]. In addition, there is an enhancement in the integrated intensity (P6) in the LVNO-1250, relative to LVNO-1000 [see Figs. 4(b, c)]. This behavior is related to the fact that the increase in the scheelite-tetragonal phase with increasing sintering temperature. These monotonous effects on the vibrational spectra are correlated to the substitution induced deformation of the VO₄³⁻ tetrahedra and is clearly reflected in the FTIR spectra of the LVNO-1250 sample [see Fig. 3(a)]. For the LVNO-1000 sample, the effects correspond to the translational vibrations of La–O bonds and the rotational motions of NbO₄³⁻ units. The peaks observed in the intermediate region (250–450 cm⁻¹) are associated with the O–V–O bending vibrations and the scissoring modes of NbO₄³⁻. Meanwhile, in the high-wavenumber region (600–900 cm⁻¹), the Raman features arise from the stretching modes of Nb–O and V–O bonds. It can be clearly seen in Fig. 4(c) that the number of vibration bonds for LVNO-1250 sample decreases in comparison to the LVNO-1000 sample, which is in agreement with the lower coordination number (8) and the high symmetry (*D*2*d*) of the La³⁺ ions in the tetragonal phase [13]. In addition, Sun *et al.* also reported that Raman peaks for the tetragonal LaVO₄ are

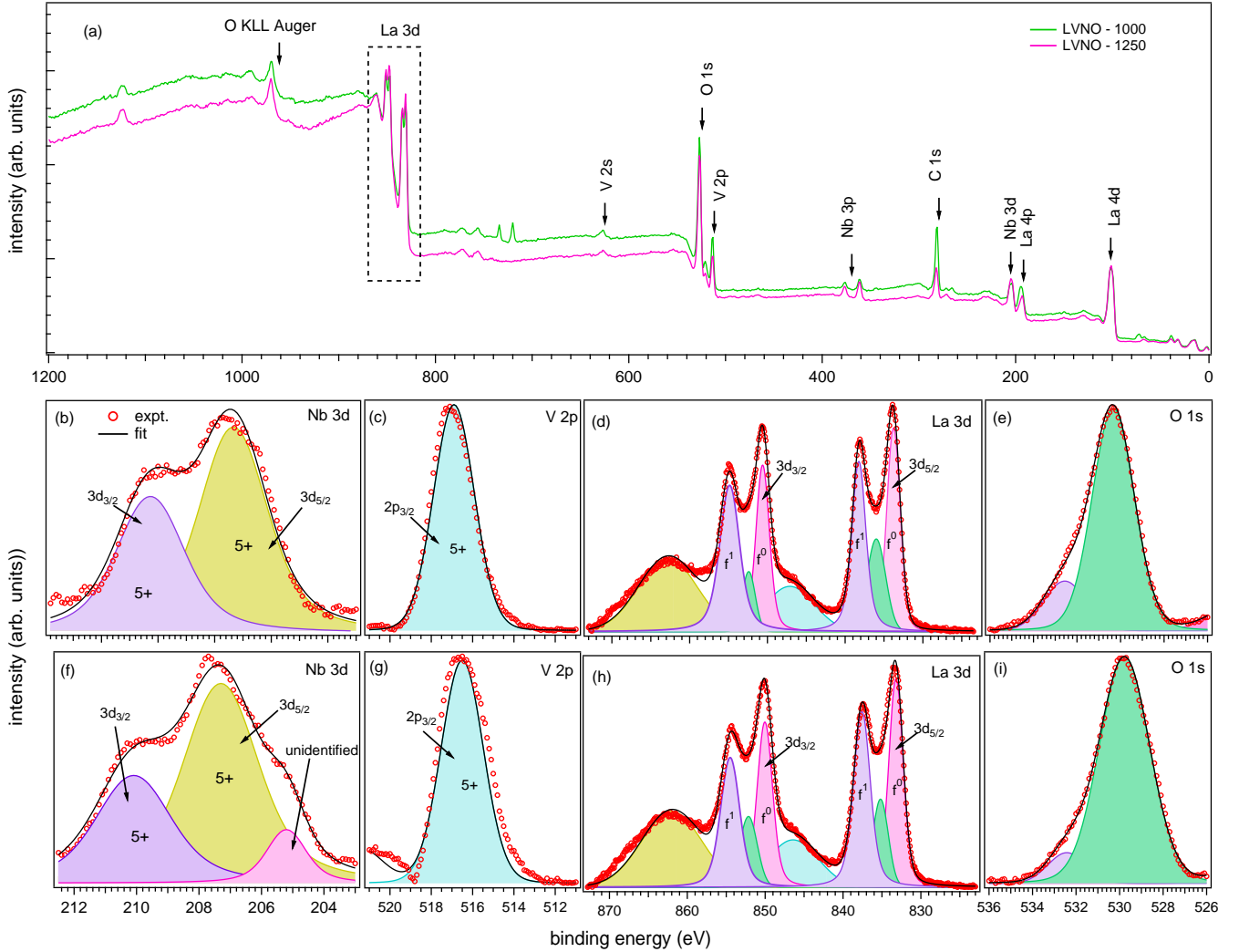


FIG. 5. (a) The room temperature XPS survey spectrum; the core level spectra of (b, f) Nb 3d; (c, g) V 2p; (d, h) La 3d and (e, i) O 1s elements of the LVNO sample sintered at 1000°C (b, c, d, e) and 1250°C (f, g, h, i), respectively.

less as compared to the monoclinic LaVO_4 due to the high symmetry ($D2d$) of La^{3+} ions, through the theoretical calculations [35].

Furthermore, the x-ray photoemission spectroscopy (XPS) is employed to probe the electronic structure by measuring the survey scan and specific elemental core-level spectra for both the samples. The detected peaks in the survey spectrum are assigned by their binding energies and exhibit strong correlation with the reported values [6], as demonstrated in Fig. 5(a). The Nb 3d core-level spectra for both the samples confirm the Nb^{5+} oxidation state [37, 38], as shown in Fig. 5(b, f). For both the samples, the Nb 3d_{5/2} and Nb 3d_{3/2} peaks are observed at around 207.3 eV and 210.2 eV, respectively, with a spin-orbit splitting of around 2.9 eV [39]. The O 1s peak [see Fig. 5(e, i)] is observed at 529.8 eV (lattice oxygen) and the energy difference between Nb 3d_{5/2} and O 1s is 322.5 eV. The O 1s peak, used as the binding-energy reference to compensate for charging

effects, is centered at 530.2 eV, giving an energy difference of 322.9 eV between the Nb 3d_{5/2} and O 1s levels [40]. There is an unidentified contribution at 205.2 eV, shown in pink color in Fig. 5(f). The energy difference of Nb 3d_{5/2} and O 1s is quite consistent, which reinforces Nb^{+5} oxidation state in both the samples.

Also, the V 2p core-level spectra for both the samples in Figs. 5(c, g), the primary V 2p_{3/2} peak occur at 516.9 eV, consistent with V^{5+} oxidation [41]. The La 3d core-level spectra for both the samples exhibit the characteristic spin-orbit splitting (3d_{5/2} and 3d_{3/2}) in Figs. 5(d, h). For the LVNO-1000 sample, the primary photoemission peaks are observed at 833.8 eV (3d_{5/2}) and 850.6 eV (3d_{3/2}), corresponding to a spin-orbit separation of 16.8 eV [42], confirming the La^{3+} oxidation state [43]. However, a double peak structure is observed in the spin-orbit component, denoted by f⁰ and f¹, corresponding to the 3d⁹f⁰ and 3d⁹f¹L configurations, shown in Figs. 5(d, h). Here, the L signifies the hole in the O 2p

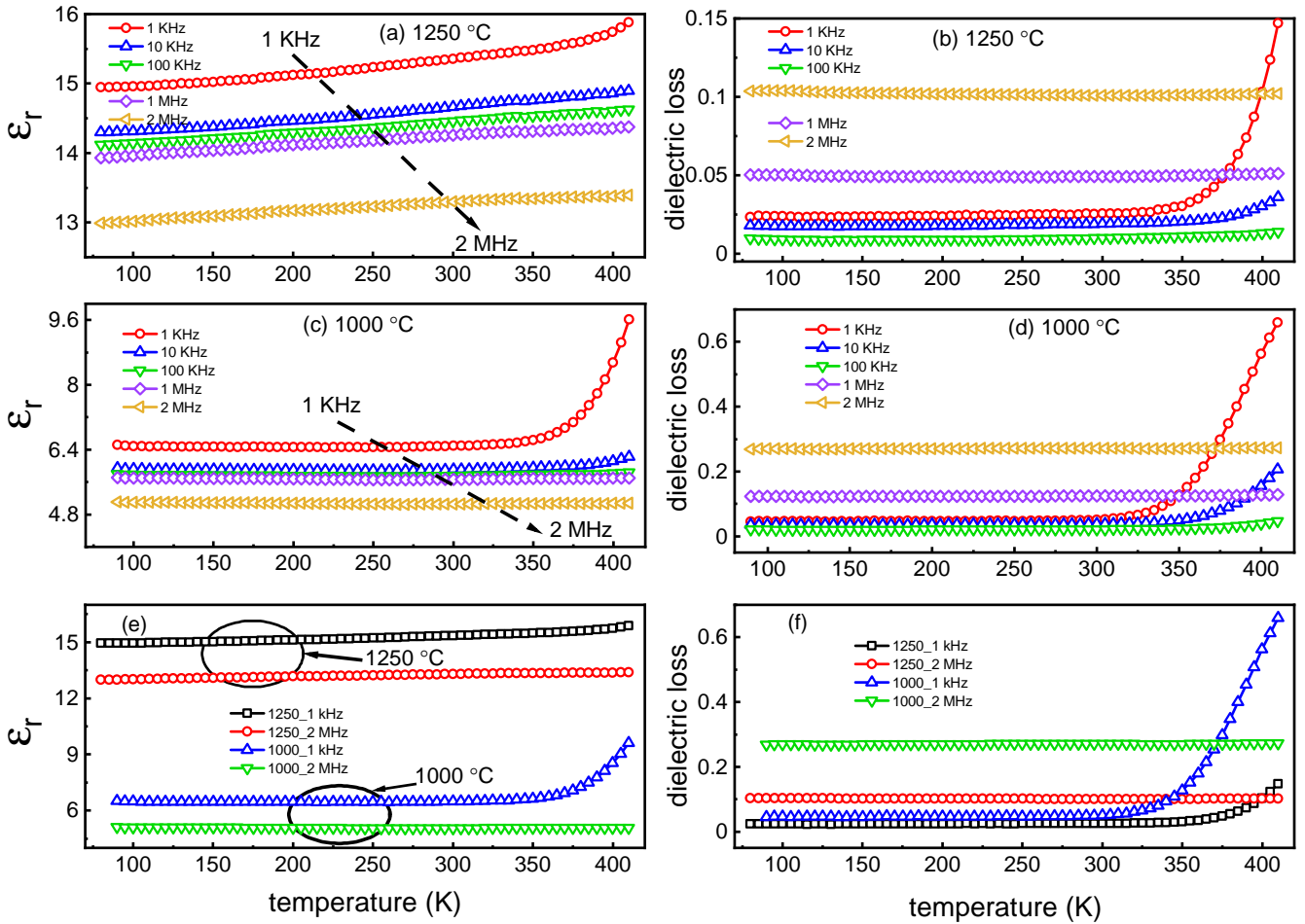


FIG. 6. The variations of electric permittivity (ϵ_r) and dielectric loss at various temperatures for selected frequencies for both the samples, sintered 1000°C and 1250°C temperatures; (a-d) the variations of electric permittivity and dielectric loss at various temperatures, (e-f) a comparison of electric permittivity and dielectric loss at two different frequencies of 1 kHz and 2 MHz, respectively. The arrow in this figure shows the direction of increasing frequency.

valence orbital and arises from the electron transfer from the ligand valence band to empty 4f orbitals [37, 44, 45]. In addition to the La 3d main peaks, broad satellite features at 847.9 and 862 eV are observed due to the plasmons [6]. For the LVNO-1250 sample, a small shift of 0.6 eV in the main La peaks toward lower binding energy is observed. The primary peaks appear at 833.2 eV ($3d_{5/2}$) and 850.0 eV ($3d_{3/2}$), with a spin-orbit splitting of 16.8 eV, while the corresponding satellite peaks occur at 837.6 eV and 854.5 eV. The energy separation between the primary and satellite peaks, which reflects the degree of metal-ligand orbital overlap [43], is calculated to be around 4.45 eV for both the samples.

Finally, the temperature dependence of dielectric permittivity and dielectric loss of the LVNO samples are shown in Fig. 6. The results show a decrease in dielectric permittivity (ϵ_r) with increasing frequency and an increase in permittivity with increasing temperature for both the samples, as shown in Figs. 6(a, c). The frequency-dependent behavior of the LVNO samples at

selected temperatures can be explained using the space charge polarization mechanism [46–48]. According to this model, at lower frequencies, the charge carriers follow the applied field, which produces a higher amount of polarization, leading to a higher permittivity. The sample sintered at 1250°C exhibit higher permittivity compared to the one sintered at 1000°C, as a higher sintering temperature leads to greater densification and larger grain size of the ceramics, which improves the accumulation of charge carriers at the interface. The higher sintering temperature, accompanied by an increase in grain size, results a decrease in insulating grain boundaries, leading to an increase in polarization and, consequently, dielectric permittivity [49, 50]. The higher amount of polarization gives rise to a large permittivity, as observed for the sample sintered at 1250°C [51, 52]. The temperature-dependent variations in permittivity are explained in terms of thermal activation of charge carriers. As the temperature is increased at a fixed frequency, the thermal energy associated with the dipoles helps them to orient

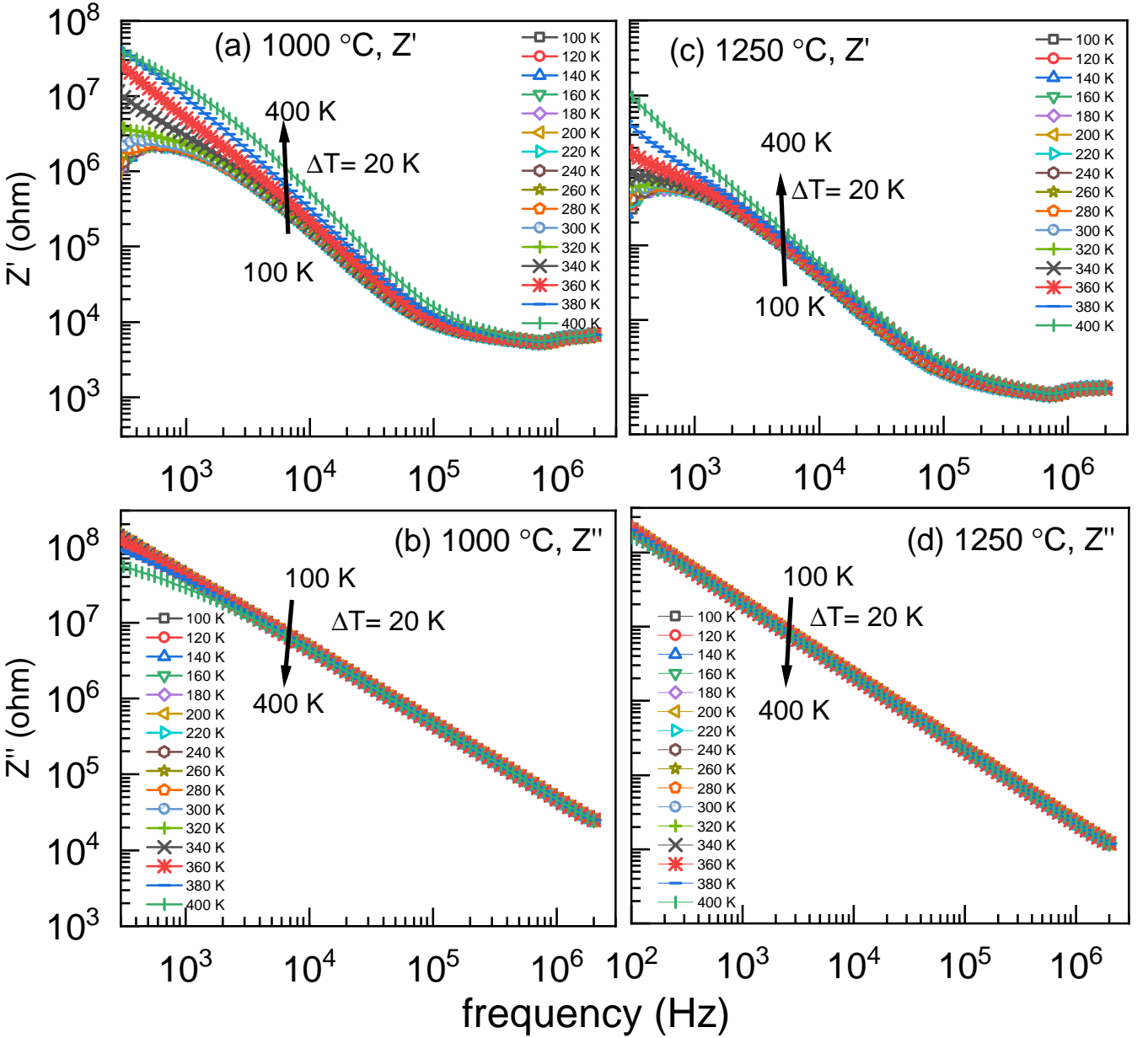


FIG. 7. The real (Z') and imaginary (Z'') parts of total impedance (Z), (a, b) for the LVNO-1000 and (c, d) for the LVNO-1250 samples. The arrow shows the direction of increasing temperatures.

along the direction of the applied field; hence, the dielectric permittivity is increased with an increase in temperature. The total dielectric permittivity is the combined effect of the applied frequency and measured temperature. A similar type of temperature-dependent behavior is also observed for the dielectric loss data, as shown in Figs. 6(b, d). The lower dielectric loss at higher sintering temperature is attributed to the greater densification (as porosity leads to dissipating the energy in dielectric materials) of the ceramics and a decrease in oxygen vacancies. An increase in dielectric loss with temperature is due to an increase in space charge polarization, which leads to an increase in conductivity of the ceramic sam-

ples, hence an enhancement in the dielectric loss. The dielectric loss at high temperature is mainly attributed to the conduction loss. The frequency-dependent dielectric loss data show an increase in dielectric loss above 100 kHz, indicating that the resonance frequency for the LVNO molecule is above 100 kHz. The comparison of dielectric permittivity Fig. 6(e) and dielectric loss Fig. 6(f) shows a higher permittivity and lower dielectric loss for sample sintered at 1250°C.

Moreover, the variation of real (Z') and imaginary (Z'') parts of total impedance at selected temperatures is shown in Fig. 7. The impedance data are normalized by

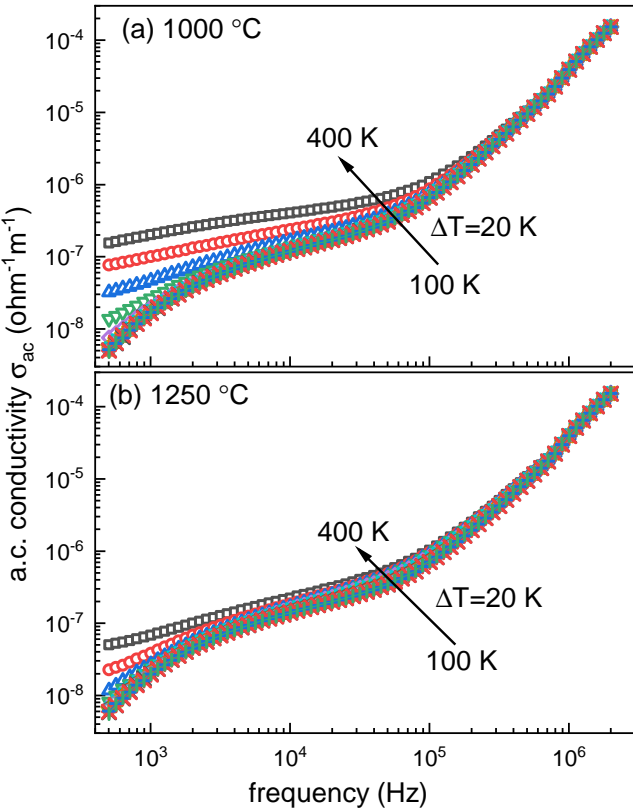


FIG. 8. The variation of ac conductivity with frequency for (a) 1000°C and (b) 1250°C sintered samples. The arrow shows the direction of increasing temperature.

the geometrical correction factor $\frac{A}{d}$, where A is the total electrode area and d is the thickness of the sample. The real part of impedance (Z') is categorized into two: (a) frequency-dependent data at lower frequencies related to the *a.c.* conduction in the material gives a rapid decrease in the impedance due to the interfacial polarization, and (b) merging of all curves with each other indicates the possible release of space charge due to reduction in potential barriers. The rapid decreasing behavior of the real impedance with frequency is due to an enhancement in the mobility of charge carriers [53]. The analysis shows that the real part of the total impedance (Z') increases with temperature, indicating the enhancement in the resistive nature of the LVNO samples, see Figs. 7(a, c). The imaginary part (Z'') decreases with temperature or nearly remains the same with temperature, indicating no variations in the capacitive nature of the samples, see Figs. 7(b, d). The higher values of impedance at lower frequencies are due to interfacial polarization, where the capacitive nature of the samples dominates according to the time constant and temperature of the samples. The sample sintered at 1250°C shows the lower values of real impedance (Z'), indicating the better crystalline nature of the sample having the lower porosity with larger grain size [54], as supported by the dielectric permittivity and

loss data shown in Fig. 6.

Note that the *a.c.* conductivity is a response of the carriers in phase with the applied electric field, which depends on the frequency of the applied field and temperature. It is a combined response of relaxation, localized hopping and diffusion of charge carriers. The variation in conductivity with frequency is a crucial tool for determining the type of carriers that dominate in the total conductivity. If the conductivity increases (decreases) with an increase in frequency, the conductivity is dominated by the contributions from the bound (free) charge carriers [46, 55–57]. In an alternating electric field, the charge carriers move from one state to another by a hopping conduction. At lower frequencies, carriers undergo long-range hopping due to the considerable time period available to them; in contrast, a shorter time period at higher frequencies results in short-range hopping. The hopping probability increases with temperature due to an increase in the activation energies of carriers as well as a reduction in barrier height, resulting in an increase in conductivity. The *a.c.* conductivity, depends also on the sample dimensions, can be calculated using the following relation [56–58]:

$$\sigma_{ac}(\omega) = \frac{t}{A} \left[\frac{Z'}{Z'^2 + Z''^2} \right] \quad (3)$$

Here, t is the thickness of the dielectric material, A is the total area of the metal electrodes, Z' and Z'' are the real and imaginary impedance of the total impedance Z .

Further, the *a.c.* conductivity calculated using equation 3 is shown in Fig. 8 at selected temperatures. The conductivity is found to increase with an increase in temperature due to the thermal activation of charge carriers; however, the conductivity remains in a similar order for samples sintered at 1000°C and 1250°C. It is found that conductivity increases with frequency for both the samples, confirming the contributions from the bound charge carriers. The conductivity data show two different types of regions: (a) a plateau-like region at lower frequencies and (b) dispersive type behavior at higher frequencies. This type of frequency-dependent variation in conductivity is explained on the basis of the Funke jump relaxation model [59]. According to this model, charge carriers follow long-range motion at lower frequencies, resulting in a frequency-independent contribution. On the other hand, at higher frequencies, the dispersive nature is due to the competition between successful and unsuccessful hopping due to the shorter time period available with carriers. The analysis shows that the discrete nature of conductivity at lower frequencies is due to the accumulation of space charge over the potential barriers, while the merging of the conductivity data at higher frequencies for both the samples confirm the reduction of potential barriers at higher frequencies due to the possible release of space charge. The sample sintered at 1000°C exhibits a large dispersive nature, as small grain size and lower densification result in a large potential barrier, thereby increasing the ratio of unsuccessful hopping to successful

hopping. On the other hand, sample sintered at 1250°C exhibit a larger grain size and higher densification, resulting in a higher amount of successful hopping over potential barriers, thus a decrease in dispersive behavior is observed. The analysis also shows that the dispersive nature shifts towards the higher frequency side with an increase in temperature for both the samples, which can be explained by the enhancement in thermal activation energy available with the carriers. At higher frequencies, lesser time scale leads to the unsuccessful hopping of carriers towards neighboring sites. As the temperature increases, the average thermal energy available to carriers is enhanced, allowing long-range hopping even for the shorter periods available at higher frequencies. The long-range hopping extends the dispersive nature towards the higher frequency side with an increase in temperature for both the samples [55, 60, 61].

IV. SUMMARY AND CONCLUSIONS

The $\text{LaV}_{0.5}\text{Nb}_{0.5}\text{O}_4$ samples were successfully synthesized via the conventional solid-state reaction route. A pronounced dependence of the physical and dielectric properties on the sintering temperatures 1000°C and 1250°C has been observed. The room-temperature Rietveld refinement of the powder X-ray diffraction patterns reveal an increase in the tetragonal phase fraction to 96%, accompanied by a minor monoclinic phase fraction of 4%, upon sintering at 1250°C. The FE-SEM analysis illustrates the surface morphology, which indicates a clear increase in particle size with increasing sintering temperature. The high-resolution transmission electron microscopy further confirms the crystallinity and coexistence of mixed phases in both

the samples. The Raman and Fourier transform infrared spectroscopy measurements validate the presence of the characteristic vibrational modes. The UV-vis diffuse reflectance spectroscopy indicates an optical band gap of 3.2 eV for the sample sintered at 1000°C; however, as the tetragonal phase becomes more prominent at 1250°C, the band gap narrows to 2.7 eV, which is advantageous for luminescent applications. The x-ray photoemission spectroscopy reveals the electronic structure and confirms the valence state of the constituent elements. Lastly, the dielectric studies reveal that the sample annealed at 1250°C exhibits higher dielectric permittivity (ϵ_r) and lower dielectric loss. These results clearly demonstrate that the sintering temperature plays a crucial role in tailoring the physical, electronic, and dielectric properties of $\text{LaV}_{0.5}\text{Nb}_{0.5}\text{O}_4$ orthovanadate.

ACKNOWLEDGMENTS

We acknowledge Physics Department at IIT Delhi for the XRD and Raman Spectroscopy measurements. The authors thank Gaurav Gupta, Vikas Joshi and Jiten Dhaka for their help during synthesis and analysis of the samples. We thank Central Research Facility (CRF) for the FESEM, EDX, HR-TEM, UV-vis DRS, FTIR and XPS measurements. The samples are synthesised in a high-temperature furnace (Nabertherm GmbH, Germany), funded by BRNS through the DAE Young Scientist Research Award (Project Sanction No. 34/20/12/2015/BRNS). RSD acknowledges SERB-DST for the financial support through a core research grant (project reference no. CRG/2020/003436).

[1] M. Yi, S. -K. Park, C.-Y. Seong, Y. Piao, and T. Yu, The general synthesis and characterization of rare earth orthovanadate nanocrystals and their electrochemical applications, *J. Alloys Compd.* **693**, 825 (2017).

[2] H. R. Xia, L. X. Li, H. J. Zhang, X. L. Meng, L. Zhu, Z. H. Yang, X. S. Liu, and J. Y. Wang, Raman spectra and laser properties of Yb-doped yttrium orthovanadate crystals, *J. Appl. Phys.* **87**, 269 (2000).

[3] M. Michalska, J. B. Jasiński, J. Pavlovsky, P. Żurek-Siwerska, A. Sikora, P. Gołębiewski, A. Szysia, V. Matejka, and J. Seidlerova, Solid state-synthesized lanthanum orthovanadate (LaVO_4) Co-doped with Eu as efficient photoluminescent material, *J. Luminescence* **233**, 117934 (2021).

[4] Z. Xu, C. Li, Z. Hou, C. Peng, and J. Lin, Morphological control and luminescence properties of lanthanide orthovanadate LnVO_4 ($\text{Ln} = \text{La to Lu}$) nano-/microcrystals via hydrothermal process, *CrystEngComm* **13**, 474 (2011).

[5] H. Dua, R. Shukla, and R. S. Dhaka, Structural phase transition and its consequences for the optical behavior of $\text{LaV}_{1-x}\text{Nb}_x\text{O}_4$, *Phys. Rev. B* **103**, 174107 (2021).

[6] A. Kumar, A. Sharma, M. Sharma, V. Singh, A. Dhaka, and R. S. Dhaka, Structural, vibrational and electronic properties of Nb substituted orthovanadates $\text{LaV}_{1-x}\text{Nb}_x\text{O}_4$, *J. Alloys Compd.* **966**, 171506 (2023).

[7] A. Kumar, V. N. Thakur, A. Kumar, V. Singh, A. Dhaka, and R. S. Dhaka, Dielectric behavior and impedance spectroscopy of Niobium substituted Lanthanum based orthovanadates at high temperatures, *Ceramics International* **50**, 6735 (2024).

[8] Shwetha. G., Kanchana V., and Vaitheeswaran G., Optical properties of orthovanadates, and periodates studied from first principles theory, *Materials Chemistry and Physics* **163**, 376 (2015).

[9] D. Errandonea, High pressure crystal structures of orthovanadates and their properties, *J. Applied Physics* **128**, 040903 (2020).

[10] V. Singh, P. Kumari, S. J. Dhoble, P. Holi, H. Jeong, and V. Koteswararao, On the green emission of holmium (III) doped LaVO_4 phosphors, *Optik* **242**, 167223 (2021).

[11] M. Toro-González, A. Peacock, A. Miskowiec, D. A. Cullen, R. Coppock, S. Mirzadeh, and S. M. Davern, Tai-

loring the radionuclide encapsulation and surface chemistry of $\text{La}^{(223)\text{Ra}}\text{VO}_4$ nanoparticles for targeted alpha therapy, *J. Nanotheranostics* **2**, 33 (2021).

[12] X. Cheng, D. Guo, S. Feng, K. Yang, Y. Wang, Y. Ren, and Y. Song, Structure and stability of monazite- and zircon-type LaVO_4 under hydrostatic pressure, *Optical Materials* **49**, 32 (2015).

[13] C. -J. Jia, L. -D. Sun, L. -P. You, X. -C. Jiang, F. Luo, Y. -C. Pang, and C. -H. Yan, Selective Synthesis of Monazite- and Zircon-type LaVO_4 Nanocrystals, *J. Phys. Chem. B* **109**, 3284 (2005).

[14] W. Fan, X. Song, Y. Bu, S. Sun, and X. Zhao, Selected-Control Hydrothermal Synthesis and Formation Mechanism of Monazite- and Zircon-Type LaVO_4 Nanocrystals, *J. Phys. Chem. B* **110**, 23247 (2006).

[15] S. W. Park, H. Kyoung Yang, J. Won Chung, Y. Chen, B. Kee Moon, B. Chun Choi, J. H. Jeong, and J. Hwan Kim, Photoluminescent properties of $\text{LaVO}_4:\text{Eu}^{3+}$ by structural transformation, *Physica B: Condensed Matter* **405**, 4040 (2010).

[16] E. Rai, R. S. Yadav, D. Kumar, A. K. Singh, V. J. Fulari, and S. B. Rai, Structural and photoluminescence properties of Cr^{3+} doped LaVO_4 phosphor, *Solid State Sciences* **129**, 106904 (2022).

[17] F. Wang, L. Yu, Y. Zhu, Z. Zhu, X. Meng, Y. Lv, S. Peng, and L. Yang, Defect control and optical performance of yttrium orthovanadate nanocrystals via a facile pH-sensitive synthesis, *J. Alloys Compd.* **968**, 172259 (2023).

[18] X. Yang, Y. Zhang, P. Zhang, N. He, Q. Yang, H. Peng, B. Zhai, and J. Gui, pH modulations of fluorescence $\text{LaVO}_4:\text{Eu}^{3+}$ materials with different morphologies and structures for rapidly and sensitively detecting Fe^{3+} ions, *Sensors and Actuators B: Chemical* **267**, 608 (2018).

[19] S. Varma, B. N. Wani, and N. M. Gupta, Synthesis, characterisation, TPR/TPO and activity studies on $\text{LaMn}_x\text{V}_{1-x}\text{O}_{4-\delta}$ -catalysts, *Appl. Catal. A: Gen.* **205** 295 (2001).

[20] H. Takei and S. Tsunekawa, Growth and properties of LaNbO_4 and NdNbO_4 single crystals, *J. Crystal Growth* **38** 55 (1977).

[21] S. Ding, H. Zhang, Y. Chen, Q. Zhang, R. Dou, W. Liu, G. Sun, and D. Sun, Structure, electronic and optical properties of LaNbO_4 : An experimental and first-principles study, *Solid State Communications* **277**, 7 (2018).

[22] A. T. Aldred, Unusual cell volume behavior in the $\text{LaNb}_{1-x}\text{V}_x\text{O}_4$ system, *Materials Letters* **1** 197 (1983).

[23] G. Blasse, and L. H. Brixner, Ultraviolet emission from ABO_4 -type niobates, tantalates and tungstates, *Chem. Phys. Lett.* **173** 409 (1990).

[24] R. D. Shannon and C. T. Prewitt, Effective ionic radii in oxides and fluorides, *Acta Crystal.* **B25**, 925 (1969).

[25] D. Guo, D. Zhou, W.-B. Li, L.-X. Pang, Y.-Z. Dai, and Z.-M. Qi, Phase Evolution, Crystal Structure, and Microwave Dielectric Properties of Water-Insoluble $(1 - x)\text{LaNbO}_4 - x\text{LaVO}_4$ ($0 \leq x \leq 0.9$) Ceramics, *Inorg. Chem.* **56**, 9321 (2017).

[26] M. Huse, A. W. B. Skilbred, M. Karlsson, S. G. Eriks-son, T. Norby, R. Haugsrud, and C. S. Knee, Neutron diffraction study of the monoclinic to tetragonal structural transition in LaNbO_4 and its relation to proton mobility, *J. Solid State Chemistry* **187**, 27 (2012).

[27] B. Xie, G. Lu, Y. Wang, Y. Guo, and Y. Guo, Selective synthesis of tetragonal LaVO_4 with different vanadium sources and its luminescence performance, *J. Alloys Compd.* **544**, 173 (2012).

[28] R. Okram, N. Yaiphaba, R. S. Ningthoujam, and N. R. Singh, Is Higher Ratio of Monoclinic to Tetragonal in LaVO_4 a Better Luminescence Host? Redispersion and Polymer Film Formation, *Inorg. Chem.* **53**, 7204 (2014).

[29] J. Li and F. L. Deepak, In situ kinetic observations on crystal nucleation and growth, *Chem. Rev.* **122**, 16911 (2022).

[30] G. Liu, X. Duan, H. Li, and H. Dong, Hydrothermal synthesis, characterization and optical properties of novel fishbone-like $\text{LaVO}_4:\text{Eu}^{3+}$ nanocrystals, *Materials Chemistry and Physics* **115**, 165 (2009).

[31] J. Tauc, R. Grigorovici, and A. Vancu, Optical properties and electronic structure of amorphous germanium, *Physica Status Solidi B* **15**, 627 (1966).

[32] V. P. Kubelka and F. Munk, Ein Beitrag zur Optik der Farbanstriche, *Z. Tech. Physik* **12**, 593 (1931).

[33] R. López and R. Gómez, Band-gap energy estimation from diffuse reflectance measurements on sol-gel and commercial TiO_2 : a comparative study, *J. Sol-Gel Sci. Technol.* **61**, 1 (2012).

[34] P. Parhi and V. Manivannan, Novel microwave initiated solid-state metathesis synthesis and characterization of lanthanide phosphates and vanadates, LMO_4 ($\text{L}=\text{Y, La}$ and $\text{M}=\text{V, P}$), *Solid State Sciences* **10**, 1012 (2008).

[35] L. Sun, X. Zhao, Y. Li, P. Li, H. Sun, X. Cheng, and W. Fan, First-principles studies of electronic, optical, and vibrational properties of LaVO_4 polymorph, *J. Appl. Phys.* **108** 093519 (2010).

[36] D. Errandonea, J. Pellicer-Porres, D. Martínez-García, J. Ruiz-Fuertes, A. Friedrich, W. Morgenroth, C. Popescu, P. Rodríguez-Hernández, A. Muñoz, and M. Bettinelli, Phase Stability of Lanthanum Orthovanadate at High Pressure, *J. Phys. Chem. C* **120**, 13749 (2016).

[37] R. Shukla, A. Jain, M. Miryala, M. Murakami, K. Ueno, S. M. Yusuf, and R. S. Dhaka, Spin dynamics and unconventional magnetism in insulating $\text{La}_{(1-2x)}\text{Sr}_{2x}\text{Co}_{(1-x)}\text{Nb}_x\text{O}_3$, *J. Physical Chemistry C* **123** 22457 (2019).

[38] R. Shukla, A. Kumar, R. Kumar, S. N. Jha, and R. S. Dhaka, X-ray absorption spectroscopy study of $\text{La}_{1-y}\text{Sr}_y\text{Co}_{1-x}\text{Nb}_x\text{O}_3$, *J. Physical Chemistry C* **125** 10130 (2021).

[39] T. Onozato, T. Katase, A. Yamamoto, S. Katayama, K. Matsushima, N. Itagaki, H. Yoshida, and H. Ohta, Optoelectronic properties of valence-state-controlled amorphous niobium oxide, *J. Phys.: Condens. Matter* **28**, 255001 (2016).

[40] V. V. Atuchin, I. E. Kalabin, V. G. Kesler, and N. V. Pervukhina, Nb 3d and O 1s core levels and chemical bonding in niobates, *J. Electron Spectroscopy and Related Phenomena* **142**, 129 (2005).

[41] G. Silversmit, D. Depla, H. Poelman, G. B. Marin, and R. De Gryse, Determination of the V2p XPS binding energies for different vanadium oxidation states (V^{5+} to V^{0+}), *J. Electron Spectroscopy and Related Phenomena* **135**, 167 (2004).

[42] D. F. Mullica, C. K. C. Lok, H. O. Perkins, and V. Young, X-ray photoelectron final-state screening in $\text{La}(\text{OH})_3$: A multiplet structural analysis, *Phys. Rev. B* **31**, 4039 (1985).

[43] V. Guigoz, L. Balan, A. Aboulaich, R. Schneider, and T. Gries, Heterostructured thin LaFeO₃/g-C₃N₄ films for efficient photoelectrochemical hydrogen evolution, *International Journal of Hydrogen Energy* **45**, 17468 (2020).

[44] R. Prakash, R. Shukla, P. Nehla, A. Dhaka, and R. S. Dhaka, Tuning ferromagnetism and spin state in La_(1-x)A_xCoO₃ (A = Sr, Ca) nanoparticles, *J. Alloys Compd.* **764**, 379 (2018).

[45] R. Shukla, and R. S. Dhaka, Anomalous magnetic and spin glass behavior in Nb substituted LaCo_{1-x}Nb_xO₃, *Phys. Rev. B* **97** 024430 (2018).

[46] R. Meena and R. S. Dhaka, Dielectric properties and impedance spectroscopy of NASICON type Na₃Zr₂Si₂PO₁₂, *Ceram. Int.* **48**, 35150 (2022).

[47] A. A. Balaraman and S. Dutta, Inorganic dielectric materials for energy storage applications: a review, *J. Phys. D Appl. Phys.* **55**, 183002 (2022).

[48] I. Ksentini, M.B. Abdessalem, W.C. Koubaa and A. Chwikhrouhou, Electrical conductivity and dielectric analysis of Ba_{0.9}Ag_{0.1}TiO₃ compound, *Appl. Phys. A* **126**, 939 (2020).

[49] Z. Sun, L. Li, H. Zheng, S. Yu and D. Xu, Effects of sintering temperature on the microstructure and dielectric properties of BaZr_{0.2}Ti_{0.8}O₃ ceramics, *Ceram. Int.* **41**, 12158 (2015).

[50] E. Chandrakala, J.P. Praveen, B.K. Hazra and D. Das, Effect of sintering temperature on structural, dielectric, piezoelectric and ferroelectric properties of sol-gel derived BZT-BCT ceramics, *Ceram. Int.* **42**, 4964 (2016).

[51] J. P. Kumar, K. S. K. R. C. Sekhar, T. D. Rao, P. D. Babu, and P. Tirupathi, Effect of sintering temperature on structural, dielectric, and electrical property studies of Bi₄NdTi₃FeO₁₅ aurivillius ceramics, *J Mater Sci: Mater Electron* **32**, 9675 (2021).

[52] M. S. Alkathy, R. Gayam and K. C. James Raju, Effect of sintering temperature on structural and dielectric properties of Bi and Li co-substituted barium titanate ceramic, *Ceram. Int.* **42**, 15432 (2016).

[53] M. Javed, A.A. Khan, N. Akbar, A. Dar and M.A. Mohmad, Low-temperature dielectric relaxation mechanism and correlated barrier hopping transport in neodymium perovskite chromite, *Mater. Res. Bull.* **165**, 112303 (2023).

[54] Y. Zhang, W. Li, S. Zhang, X. Tang, Q. Liu and X. Guo, The dielectric relaxation and impedance spectroscopy analysis of (Bi_{0.5}Na_{0.5})TiO₃-based ceramics, *Mater. Res. Bull.* **153**, 111874 (2022).

[55] S. Sumi, P. P. Rao, M. Deepa and P. Koshey, Electrical conductivity and impedance spectroscopy studies of cerium-based aeschynite type semiconducting oxides: CeTiMO₆ (M = Nb or Ta), *J. Appl. Phys.* **108**, 063718 (2010).

[56] R. Meena and R.S. Dhaka, Temperature dependent conductivity, dielectric relaxation, electrical modulus and impedance spectroscopy of Ni substituted Na_{3+2x}Zr_{2-x}Ni_xSi₂PO₁₂, *Phys. B: Cond. Matter.* **690**, 416209 (2024).

[57] R. Meena and R.S. Dhaka, Structural and electrical transport properties of NASICON type Na₃Zr_{2-x}Ti_xSi₂PO₁₂ solid electrolyte materials, *Small* **21**, 2501197 (2025).

[58] S. Raut, P. D. Babu, R. K. Sharma, R. Pattanayak and S. Panigrahi, Grain boundary dominated electrical conduction and anomalous optical-phonon behavior near the neel temperature in YFeO₃ ceramics, *J. Appl. Phys.* **123**, 174101 (2011).

[59] K. Funke, Jump relaxation in solid electrolytes, *Prog. Solid State Chem.* **22**, 111 (1993).

[60] T. L. Rao, M. K. Pradhan, V. Siruguri and S. Dash, Doping-Induced Modifications in the Magnetoelectronic Properties in LaFeO₃ Nanoparticles, *J. Super. Cond. Mag.* **33**, 1593 (2020).

[61] Y. Moualhi, M. Smari, H. Rahmouni, K. Khirouni, E. Dhahri, Superlinear dependence of the conductivity, double/single Jonscher variations and the contribution of various conduction mechanisms in transport properties of La_{0.5}Ca_{0.2}Ag_{0.3}MnO₃ manganite, *J. Alloy. Compd.* **898**, 162866 (2022).